

Unusual magnetotransport behavior of the martensitic compound GdPd₂BiSnehashish Chatterjee, Saurav Giri, and Subham Majumdar ^{*}*School of Physical Sciences, Indian Association for the Cultivation of Science, 2A & B Raja S. C. Mullick Road, Jadavpur, Kolkata 700032, India*Prabir Dutta *Jawaharlal Nehru Centre for Advanced Scientific Research, Jakkur, Bangalore 560064, India*Surasree Sadhukhan and Sudipta Kanungo [†]*School of Physical Sciences, Indian Institute of Technology Goa, Ponda 403401, Goa, India*Souvik Chatterjee *UGC-DAE Consortium for Scientific Research, Kolkata Centre, Sector III, LB-8, Salt Lake, Kolkata 700106, India*Manju Mishra Patidar,[‡] Gunadhor Singh Okram, and V. Ganesan[§]*UGC-DAE Consortium for Scientific Research, University Campus, Khandwa Road, Indore 452017, India*G. Das ^{||} and V. Rajaji*Chemistry and Physics of Materials Unit, Jawaharlal Nehru Centre for Advanced Scientific Research, Jakkur, Bangalore 560064, India*

(Received 5 December 2022; accepted 14 August 2023; published 23 August 2023)

This paper aims to address the structural, magnetic, electronic, and thermal properties of the rare-earth-based Heusler compound GdPd₂Bi. Our experimental findings indicate that our sample orders antiferromagnetically below the Néel temperature $T_N = 9$ K. Resistivity versus temperature data show a sharp jump below about 175 K upon cooling, which is also associated with thermal hysteresis. This is further supported by specific heat and thermopower measurements, although no such signature is observed in the magnetization study. Temperature-dependent powder x-ray diffraction measurements confirm a martensitic transition around the region of thermal hysteresis (~ 175 K) from the high-temperature (HT) cubic Heusler $L2_1$ structure to the low-temperature (LT) orthorhombic $Pmma$ structure similar to many previously reported shape memory alloys. We observe robust Bain distortion between cubic and orthorhombic lattice parameters, related by $a_{\text{orth}} = \sqrt{2}a_{\text{cub}}$, $b_{\text{orth}} = a_{\text{cub}}$, and $c_{\text{orth}} = a_{\text{cub}}/\sqrt{2}$, that occurs by contraction along the c axis and elongation along the a axis, respectively. The sample shows an unusual “nonsaturating” H^2 -dependent negative magnetoresistance for magnetic field as high as 150 kOe, and such behavior can be accounted for by the Gd $4f$ - $5d$ interaction leading to the polarization of the $5d$ band. In addition, nonlinear field dependence of the Hall resistivity is observed below about 30 K, which coincides with the sign change of the Seebeck coefficient. The electronic structure calculations confirm metallic states in both the LT and HT phases. This indicates the complex nature of the Fermi surface along with the existence of both electron and hole charge carriers. The anomalous transport behaviors can be related to the presence of both electrons and holes at the Fermi surface.

DOI: [10.1103/PhysRevB.108.075154](https://doi.org/10.1103/PhysRevB.108.075154)**I. INTRODUCTION**

Heusler-based intermetallic alloys and compounds continue to be in the forefront of active research due to

their multifaceted electronic and magnetic properties. They have already been identified as material for the development of spintronics devices, magnetic actuators, and switches [1–4]. So far, the major attention has been given to 3d-transition-metal-based Heusler compounds [5]. Early studies of the rare-earth-based (R -based full-Heusler compounds were reported for Pd₂DySn and Pd₂HoSn, which were found to order antiferromagnetically below 5 K [6–8]. On the other hand, members of the Pd₂RSn ($R = \text{Tm, Lu, Y, Yb}$) family were found to be superconducting [6]. Recently, rare-earth-bismuth-based full-Heusler compounds and half-Heusler compounds have attracted huge attention for their potential contribution in the field of spintronics. A number of

^{*}sspsm2@iacs.res.in[†]sudipta@iitgoa.ac.in[‡]Present address: Emerald Heights International School, A.B. Road, Rau, Indore 453331, India.[§]Present address: Medi-Caps University, A.B. Road, Pigdamber, Rau, Indore 453331, India.^{||}Present address: Elettra Sincrotrone Trieste, Strada Statale 14, km 163.5 in AREA Science Park, Basovizza, Trieste 34149, Italy.

RPdBi and RPtBi compounds are reported to have nontrivial band topology [9,10]. Most importantly, RPtBi and RPdBi are identified as Weyl semimetals showing the anomalous Hall effect due to the Berry curvature [11,12].

Close relatives to the RPdBi series are the RPd_2Bi -type full-Heusler compounds. However, unlike the half-Heusler compounds, RPd_2Bi compounds possess inversion symmetry. Most of them either order antiferromagnetically at low temperature (below 10 K) or show a nonmagnetic ground state [13,14]. The Dy, Ho, and Er compounds in the series show the additional signature of a first-order phase transition in the resistivity versus temperature data around 100–150 K [13]. For the Ho compound, the first-order phase transition is found to be associated with a structural change as evident from the appearance of additional peaks in the temperature-dependent x-ray diffraction data [14]. To the best of our knowledge, there is no report of the magnetic and transport properties of GdPd₂Bi in the literature.

Gd has total angular momentum $J = S = 7/2$ due to the half-filled $4f$ shell, which implies that the magnetocrystalline anisotropy will be weaker. In this paper, we have performed a comprehensive study on GdPd₂Bi through our magnetic, transport, and structural investigations along with density-functional-theory-based (DFT-based) electronic structure calculations. Though there are several reports on the electronic structure of RPdBi and RPtBi compounds, the full-Heusler-based RPd_2Bi compounds have hardly been investigated through *ab-initio*-based electronic structure calculations. Our work identifies a martensitic-type structural transition in the compound from a cubic $L2_1$ structure to an orthorhombic $Pmma$ structure below about 150 K. The compound shows unconventional negative magnetoresistance and nonlinear field variation of Hall coefficient, which can be attributed to the presence of a multiband electronic structure.

II. EXPERIMENTAL DETAILS

A polycrystalline sample of GdPd₂Bi was prepared using the conventional arc-melting technique, and the as-cast ingot was used for further measurements. The phase purity and the crystallographic structure were ensured by powder x-ray diffraction (PXRD) followed by Rietveld refinement, which was performed using the MAUD software package [15]. Rietveld refinement of the PXRD pattern obtained at room temperature confirms the formation of MnCu₂Al-type $L2_1$ structure (space group $Fm\bar{3}m$). The refined cubic lattice parameter is found to be 6.812(6) Å.

Magnetic measurements were carried out by using a commercial Quantum Design superconducting quantum interference device (SQUID) magnetometer (MPMS-XL EverCool model). Hall resistivity ρ_{xy} and the normal longitudinal resistivity $\rho = \rho_{xx}$ were measured on a cryogen-free high-magnetic-field system (Cryogenic, London) between 5 and 300 K in the presence of magnetic field as high as 150 kOe. Thermopower measurement was performed in a laboratory-based setup using the differential technique between 10 and 300 K. The sample was further investigated through high-resolution temperature-dependent x-ray diffraction (the wavelength of the radiation being 0.749 Å) using the synchrotron facility at the Photon Factory, National Laboratory

for High Energy Physics (KEK), Tsukuba, Japan, at various sample temperatures ranging from 15 to 300 K. Heat capacity C_p measurement was carried out using a Quantum Design Physical Properties Measurement System.

III. THEORETICAL TECHNIQUES

DFT-based electronic structure calculations were performed using the plane-wave basis set based on a pseudopotential framework as incorporated in the Vienna *ab initio* simulation package (VASP) [16,17]. The exchange-correlation functional was employed following the Perdew-Burke-Ernzerhof (PBE) prescription [18]. The effect of the spin-orbit coupling (SOC) is introduced as a fully relativistic correction term to the Hamiltonian. For the plane-wave basis, a 350-eV cutoff was applied. To take care of the missing on-site Coulomb interaction, we have used $U_{\text{eff}} = 6$ eV for Gd, where $U_{\text{eff}} = U - J_H$, U is the on-site Coulomb interaction, and J_H is the Hund's coupling term [19,20]. The structural optimization was performed by relaxing the internal atomic positions toward equilibrium until the Hellmann-Feynman force becomes less than 0.001 eV/Å. A k -point mesh of $6 \times 6 \times 6$ in the Brillouin zone (BZ) was used, and the electronic convergence criteria were set to be at 10^{-7} eV for self-consistent calculations.

IV. EXPERIMENTAL RESULTS

A. Magnetization

GdPd₂Bi is found to order antiferromagnetically at $T_N = 9$ K as shown in Fig. 1(a). A weak bifurcation between field-cooled (FC) and zero-field-cooled (ZFC) magnetizations was observed below about 4 K. The dc magnetic susceptibility $\chi = M/H$ (M and H are the magnetization and the applied magnetic field, respectively) between 20 and 300 K can be well fitted with the Curie-Weiss law: $\chi(T) = C/(T - \theta_p)$, where C is the Curie constant and θ_p is the paramagnetic (PM) Weiss temperature. From the good fitting of the χ vs T data [see inset of Fig. 1(a)], we get the effective PM moment, $\mu_{\text{eff}} = 8.0 \mu_B/\text{f.u.}$ and $\theta_p = -18$ K. The half-filled $4f$ shell of the free Gd³⁺ has the effective moment 7.9 $\mu_B/\text{f.u.}$, which is close to the observed value. The negative value of θ_p indicates the predominant antiferromagnetic (AFM) correlation in the system. The isothermal magnetization curves [Fig. 1(b)], measured up to $H = 70$ kOe, are found to be linear at $T = 5, 10,$ and 150 K. The linear isotherm even at 5 K supports the AFM nature of the magnetic ordering.

B. Electrical resistivity

The most fascinating observation in this paper is obtained from the transport measurements. The T variation of ρ for GdPd₂Bi in the presence of $H = 0$ and 100 kOe is presented in Figs. 2(a) and 2(b), respectively. The sample shows the conventional decrease in ρ with temperature down to around $T = 180$ K. Upon further cooling, ρ follows an upturn with decreasing T down to around 30 K, and eventually it shows a saturating tendency. The region of upturn shows clear thermal hysteresis indicating the transition to be first order in nature. A similar upturn was previously observed in the cases of other

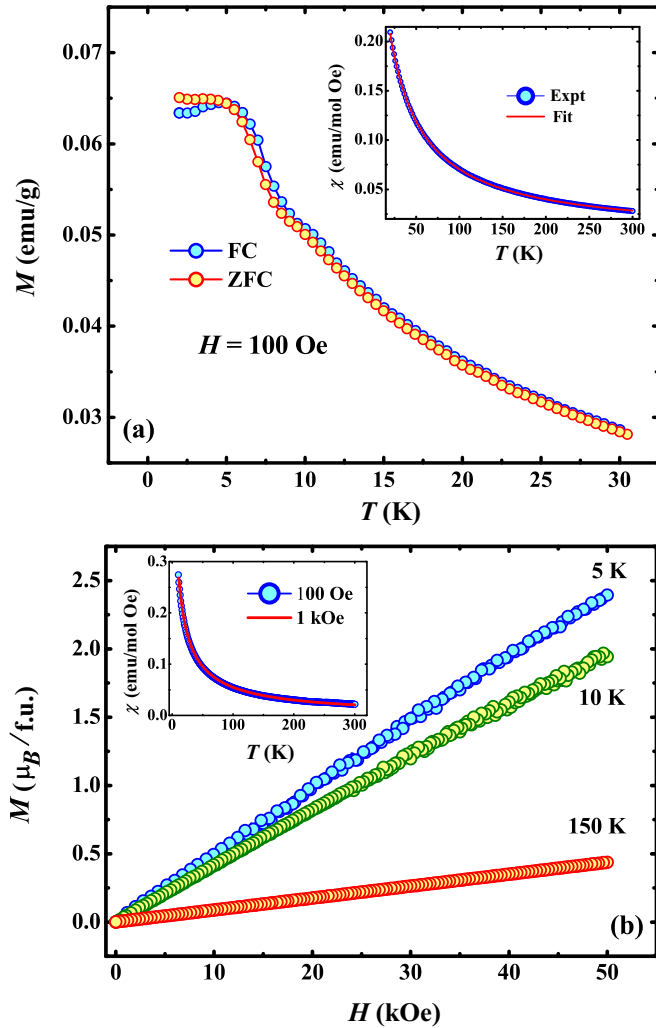


FIG. 1. (a) M vs T curve measured at $H = 100$ Oe in both ZFC and FC protocols for GdPd_2Bi . Inset: magnetic susceptibility vs temperature data along with the Curie-Weiss fit. (b) Isothermal magnetization data measured at different temperatures. Inset: magnetic susceptibility vs temperature data for $H = 100$ Oe and 1 kOe.

members of the family, namely, HoPd_2Bi and DyPd_2Bi [13]. Since we do not observe any features between 100 and 200 K in the M vs T data, the observed transition is likely to be purely structural in nature. Notably, the signature of the AFM ordering around 9 K is also present in the zero-field $\rho(T)$ data [see the inset of Fig. 2(a)].

The thermal hysteresis and the upturn survive even under an applied field of 100 kOe, and there is no significant change in the position of the upturn and the width of the thermal hysteresis. However, a clear drop in ρ is observed below about 30 K [as evident from Fig. 2(b)] signifying negative magnetoresistance (MR), which indicates the emergence of a magnetic-field-induced metallicity in GdPd_2Bi . The peak due to the AFM ordering in zero field [inset of Fig. 2(a)] vanishes for $H \geq 20$ kOe. The inset of Fig. 2(b) shows the ρ versus T^2 plot below $T = 20$ K for different values of H . The system deviates completely from T^2 behavior for $H < 20$ kOe. It is evident that $\rho(T)$ follows a T^2 dependence for $H = 100$ kOe below about 16 K, while similar T^2 variation is observed be-

low 14 K for $H = 50$ kOe. Such variation of ρ in a PM state is commonly attributed to the electron-electron scattering in the Fermi liquid (FL) theory of metals. The coefficient of the T^2 term is found to be $A = 1.3 \times 10^{-8}$ and $2.4 \times 10^{-8} \Omega \text{ cm K}^{-2}$ at 100 and 50 kOe, respectively. The value of A is about one order of magnitude higher than that for the conventional metals such as Cu [21].

The region of upturn in the $\rho(T)$ data around 175 K is associated with the negative temperature coefficient of resistivity [$d\rho(T)/dT < 0$], and such behavior is generally observed in insulators, semiconductors, or semimetals. However, the present rise can be ascribed to the structural transition, which is evident from our later analysis.

To shed more light on the occurrence of field-induced metallicity below 30 K, we measured the field variation of ρ up to ± 150 kOe at $T = 5$ and 10 K that eventually leads to a large negative magnetoresistance ($\text{MR} = [\rho(H) - \rho(0)]/\rho(0)$) of around -16 and -9% , respectively. Hence a conventional positive contribution from the Lorentz force can be ruled out for GdPd_2Bi . Interestingly, the negative MR in the bulk GdPd_2Bi sample is “nonsaturating” in nature and follows the form $-\frac{\Delta\rho}{\rho} \propto H^2$ [Fig. 2(c)] for H as high as 150 kOe. In addition, the negative MR persists in the compound for T as high as 120 K, which is much higher than T_N , although the magnitude of MR decreases with increasing T [Fig. 2(d)].

C. Heat capacity

Figure 3(a) presents the low-temperature $C_p(T)$ data measured in zero magnetic field as well as under $H = 60$ kOe. The zero-field data show a clear λ -like anomaly around 9 K, which matches well with the AFM transition observed in the magnetization data. Under the application of 60 kOe magnetic field, the transition does not get suppressed, albeit the peak slightly shifts towards lower T (8 K). We have also calculated the change in entropy (ΔS) due to the application of H (magnetocaloric effect) [22] around T_N using the following relation:

$$\Delta S(T) = \int_0^T [C_p(H)/T - C_p(0)/T] dT. \quad (1)$$

$\Delta S(T)$ is found to be negative with a sharp anomaly at the magnetic transition temperature [inset of Fig. 3(a)]. ΔS attains a moderate value of magnitude $2 \text{ J kg}^{-1} \text{ K}^{-1}$ at T_N , which is apparently connected to the field-induced shift of T_N to lower T .

At high temperature, the C_p vs T data show a peak around $T_p = 162$ K for both 0- and 60-kOe measurements [Fig. 3(b)]. The peak in C_p occurs around the temperature where the upturn in the $\rho(T)$ data is observed. Such a feature is associated with the structural phase transformation as mentioned in Sec. IV F. The nature of the C_p vs T curve around T_p does not show any change due to the application of H . Interestingly, the heating and the cooling data of $C_p(T)$ show thermal hysteresis around this structural transition, which mimics the similar observation in the $\rho(T)$ measurements. The C_p value at 300 K is found to be pretty close to the classical Dulong-Petit limit [$= 3pR$, where R is the universal gas constant and p ($= 4$ here) is the number of atoms per formula unit] ($\sim 100 \text{ J mol}^{-1} \text{ K}^{-1}$).

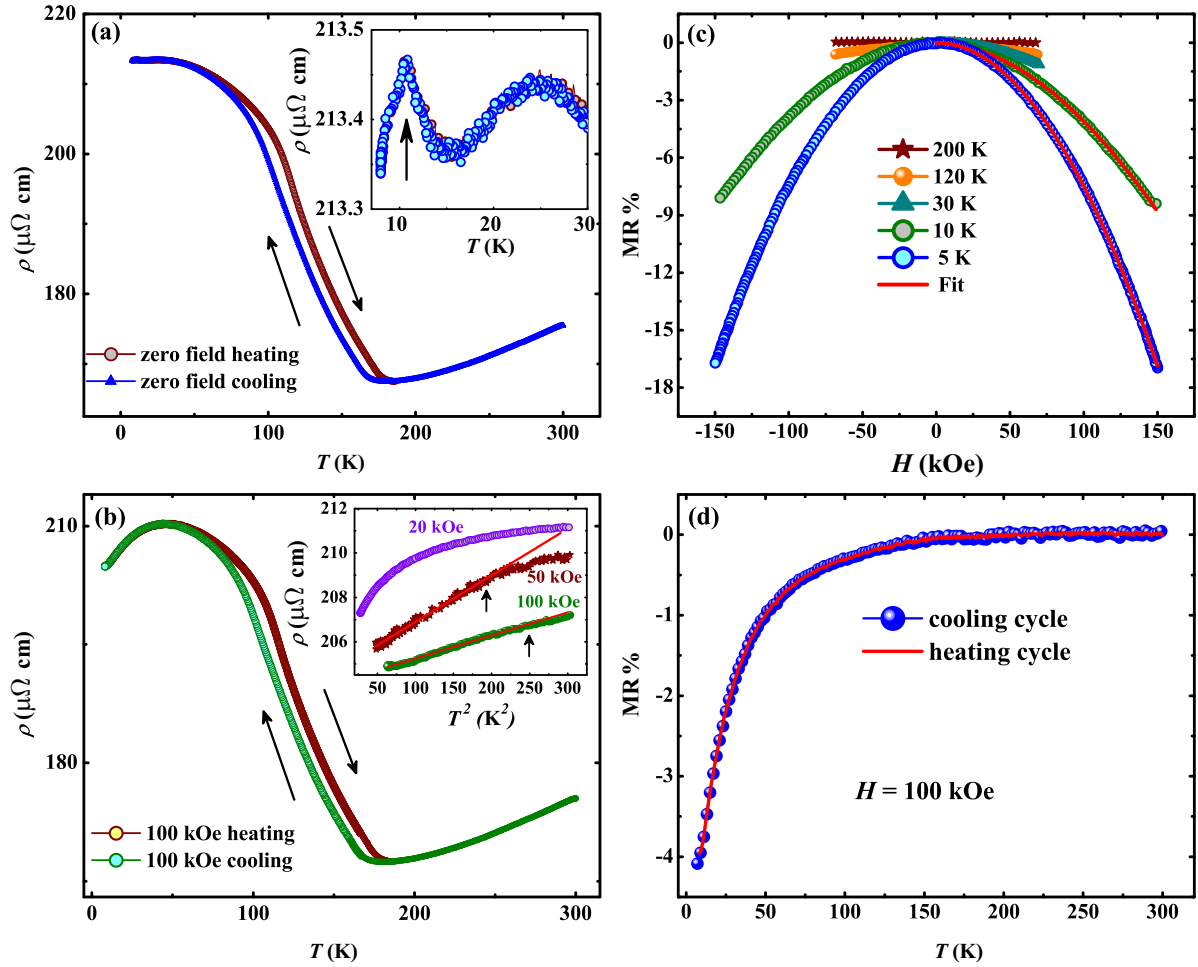


FIG. 2. The electrical resistivity as a function of temperature at (a) $H = 0$ kOe and (b) 100 kOe for GdPd₂Bi. The inset in (a) shows an enlarged view of the low- T region of $\rho(T)$ measured at $H = 0$ kOe, and the inset in (b) shows the T^2 behavior of the low- T regime at different H . (c) The magnetoresistance as a function of applied magnetic field measured at different constant temperatures. The red line is the H^2 fit to the magnetoresistance data. (d) The magnetoresistance as a function of temperature measured at $H = 100$ kOe.

D. Thermopower

We have performed the thermopower measurement in terms of the Seebeck coefficient α_S [23] in zero field as shown in Fig. 4. GdPd₂Bi shows a negative value of α_S between 25 and 270 K attaining a maximum value with magnitude ~ 3 $\mu\text{V}/\text{K}$. $\alpha_S(T)$ shows a humplike feature around 150 K, which matches well with the region of thermal hysteresis in the $\rho(T)$ data. Interestingly, α_S changes its sign and turns positive below 25 K, and it attains a value of ~ 1 $\mu\text{V}/\text{K}$ at 12 K, which may be due to the presence of both electrons and holes in the system. In a two-carrier system the thermopower is often expressed as

$$\alpha_S = \frac{\sigma_h \alpha_{S,h} + \sigma_e \alpha_{S,e}}{\sigma_h + \sigma_e}, \quad (2)$$

where σ is the electrical conductivity and the subscripts h and e denote the hole and electron contributions, respectively. Thus Eq. (2) makes it clear that $\alpha_S(T)$ might exhibit change in sign with temperature if both electrons and holes are present [24]. We find that GdPd₂Bi is the only compound in the RPd_2Bi series which predominantly shows a negative value of α_S [13]. On the other hand, RPd_2Sb compounds show a nega-

tive α_S value, but they do not undergo any structural transition (lack of thermal hysteresis) [13,25]. Bi-based compounds are often found to be potential candidates for thermoelectric applications [26]. However, in the case of GdPd₂Bi, the power factor (PF) is rather low (~ 25 $\mu\text{W m}^{-1} \text{K}^{-2}$).

E. Hall measurements

The Hall resistivity ρ_{xy} for GdPd₂Bi was determined as the antisymmetric part of the measured transverse voltage, $\rho_{xy} = t[V_{xy}(+H) - V_{xy}(-H)]/2I$, where t is the thickness of the sample, I is the applied current, and V_{xy} is the transverse voltage generated. The variation of ρ_{xy} with H measured at different constant temperatures up to $H = 70$ kOe is depicted in Fig. 5(a) [27,28]. The negative value of ρ_{xy} at all measured temperatures indicates the electron to be the majority carrier in the system. As the temperature is lowered from room temperature, the ρ_{xy} vs H plot shows linear variation above about 30 K. However, upon further lowering of T , ρ_{xy} turns nonlinear for $T \leq 30$ K suggesting that a simple picture of the single-carrier model for the conventional Hall effect is inadequate for the sample, at least below 30 K.

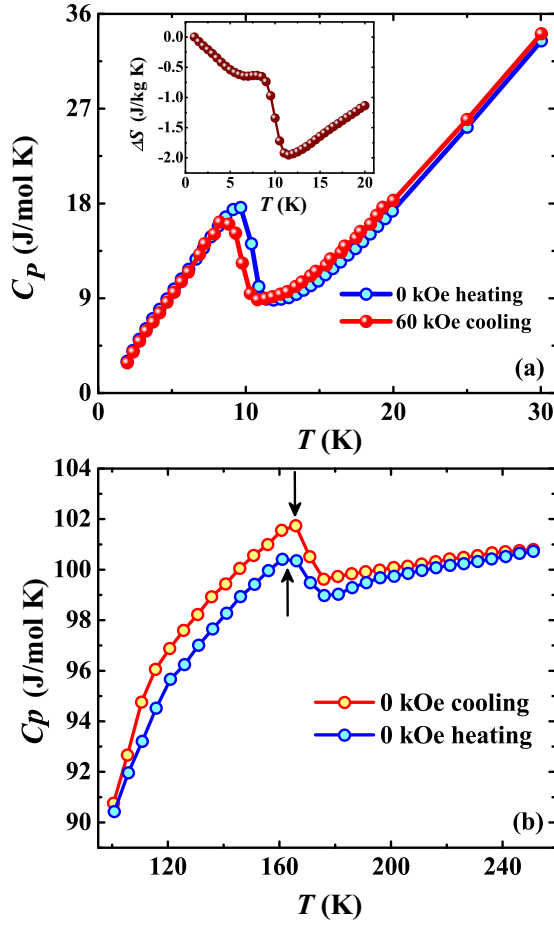


FIG. 3. Heat capacity C_p as a function of temperature in the ranges (a) 2–30 K and (b) 100–200 K measured under 0 and 60 kOe for GdPd₂Bi. The inset of (a) shows the ΔS vs T plot.

We have depicted the T variation of ρ_{xy}/H in the inset of Fig. 5(a), and it is strongly T dependent along with a clear anomaly around the temperature of thermal hysteresis observed in the $\rho(T)$ data.

As mentioned earlier, the low- T Hall resistivity ($T = 5, 10,$ and 30 K) shows a nonlinear nature and follows a concave-upward shape as can be seen from Fig. 6. The nonlinearity at low T may arise either due to the presence of more than one charge carrier or due to the anomalous Hall contribution [29]. Since the sample shows a perfect linear variation of M with H (see upper inset of Fig. 1), the nonlinearity of the $\rho_{xy}(H)$ cannot be simply attributed to the anomalous Hall effect (AHE) of magnetic origin. Notably, α_S turns from negative to positive below about 25 K. Such behavior may be due to the presence of both electrons and holes in the system. Therefore a multiband model consisting of holes and electrons seems logical to describe the nonlinearity in ρ_{xy} . This is also supported by the theoretical calculations presented later.

We invoked the following two-carrier model to fit the Hall resistivity [30]:

$$\rho_{xy}(H) = \frac{H}{e} \left[\frac{(n_h \mu_h^2 - n_e \mu_e^2) + (n_h - n_e)(\mu_h^2 \mu_e^2) H^2}{(n_h \mu_h + n_e \mu_e)^2 + (n_h - n_e)^2 \mu_h^2 \mu_e^2 H^2} \right]. \quad (3)$$

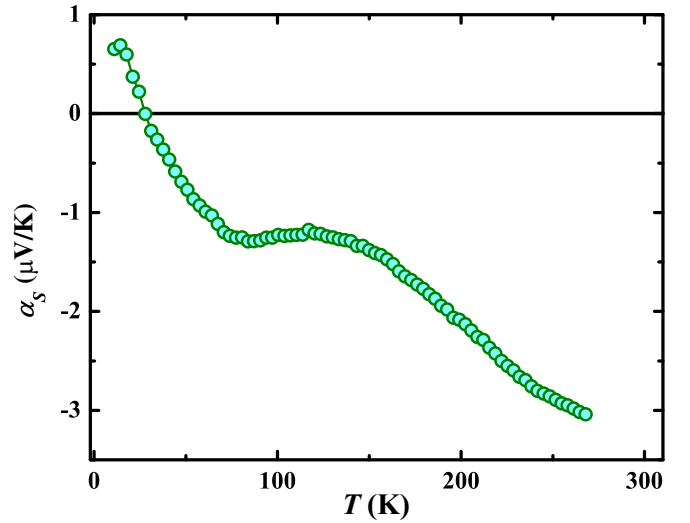


FIG. 4. Seebeck coefficient as a function of temperature for GdPd₂Bi.

Here, n_h (n_e) and μ_h (μ_e) are the carrier density and mobility of holes (h) [electrons (e)], respectively. As can be seen from Fig. 6, ρ_{xy} for $T = 5, 10,$ and 30 K can be fitted with Eq. (3) suggesting that the two-carrier model can successfully describe the experimentally measured data below about 30 K. However, the linear nature of ρ_{xy} versus H above 30 K prompted us to express the Hall resistivity data via an effective single-carrier model, where the normal Hall coefficient [$R_H = \rho_{xy}(H)/H$] is calculated from the slope of the high-field ($40 \text{ kOe} < H < 70 \text{ kOe}$) data [31,32].

The T variation of the carrier concentration and the T variation of the Hall mobility are shown in Fig. 5(b). For $T \geq 50$ K (region II), the figure shows only the electronic carrier concentration, $n_{\text{tot}} = n_e$, because we have used a single-carrier (electron) model in this temperature range. Below about 30 K, we have shown both n_e and n_h as well as the total value $n_{\text{tot}} = n_e + n_h$ (region I). Clearly, the carrier concentration shows a decreasing trend below about 30 K. The extracted value of n_{tot} increases from $1.9 \times 10^{21} \text{ cm}^{-3}$ at 5 K (derived from the two-carrier model) to $7 \times 10^{21} \text{ cm}^{-3}$ at room temperature, which is in line with what is typical for semimetallic materials [33,34]. The Hall mobility μ_H is also deduced from the linear fitting of the ρ_{xy} data above 50 K using the equation $\mu_H = R_H/\rho(H=0)$. μ_H is found to be almost T independent with a value close to $4 \text{ cm}^2 \text{ V}^{-1} \text{ s}^{-1}$ [see inset of Fig. 5(b)].

For the sake of completeness, we measured ρ_{xy} up to 150 kOe at 5 K. The ρ_{xy} versus H data are still found to be nonlinear even above 70 kOe. The values of n_e and n_h are found to be similar to those obtained previously from the data with maximum field of 70 kOe.

F. Temperature evolution of structural parameters

The results from synchrotron-based PXRD performed at different constant temperatures are plotted in Fig. 7(a). They show [see Figs. 7(a) and 7(b)] a change in the pattern as T is lowered from 300 to 15 K. To highlight the change, the T evolution of the most intense (220) peak of the cubic phase is shown in Fig. 7(b). Splitting of the main peak with the

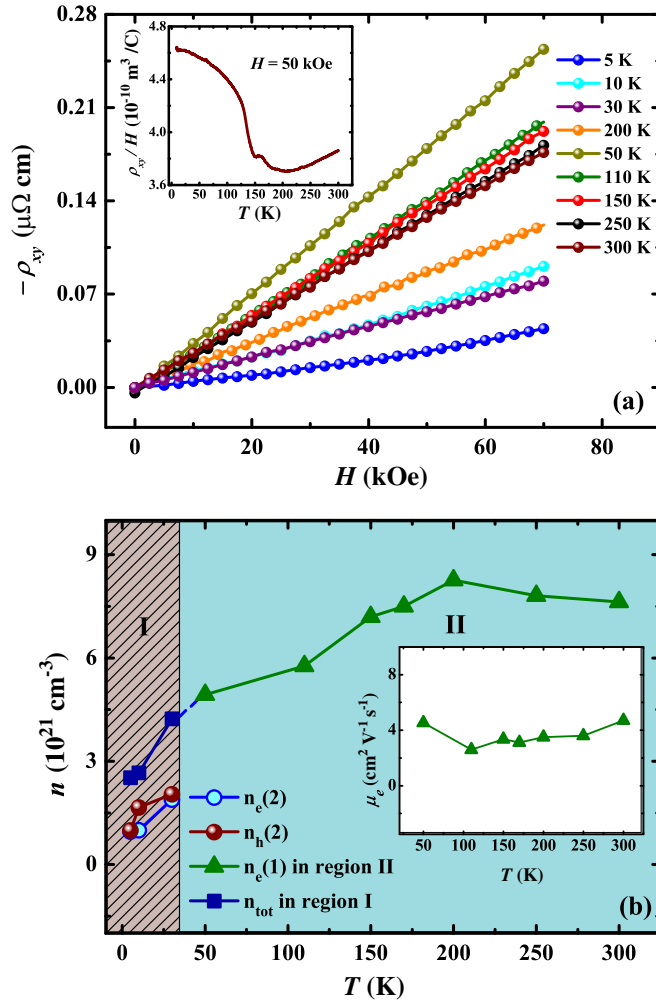


FIG. 5. (a) ρ_{xy} vs H at different constant temperatures. The inset shows the T variation of ρ_{xy}/H for $H = 50$ kOe. (b) T variation of the carrier concentration. In region I, a two-band model is used to calculate electron and hole concentrations (n_e and n_h , respectively), and the blue line with square symbols shows the total carrier density ($n_{\text{tot}} = n_e + n_h$). In region II, the concentration for a single carrier (electron) is calculated. Inset: T variation of the Hall mobility for GdPd₂Bi. $n_{e,h}(i)$ and $\mu_{e,h}(i)$ denote the carrier concentration and carrier mobility obtained from single-carrier ($i = 1$) and two-carrier ($i = 2$) models, respectively.

decrease in T is consistent with the loss of cubic symmetry, and the structure presumably attains a lower symmetry. Earlier, Gofryk *et al.* proposed the existence of a structural transition in the RPd₂Bi series of compounds [13], and the low- T crystal structure was reported to be orthorhombic ($Pnma$) [14]. We have carefully analyzed the data using the Rietveld refinement technique, and the fitted data for the representative temperature 15 K are shown in Fig. 7(c). We used ISODISTORT [35,36] software to identify a list of all the possible noncubic, nonisomorphic subgroups of the parent cubic structure. We find that the orthorhombic $Pnma$ structure generates all the experimentally observed reflections correctly and these reflections converge well with the data. In the intermediate temperatures, both cubic and orthorhombic structures [see Figs. 8(c) and 8(d)] coexist, and we have considered both

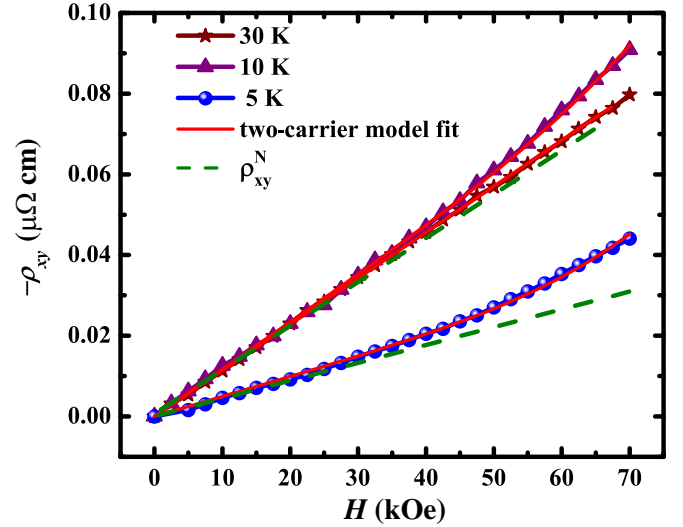


FIG. 6. ρ_{xy} vs H for $T = 5, 10,$ and 30 K along with the fit of the two-carrier model [Eq. (3)]. ρ_{xy}^N denotes the linear normal Hall contribution.

the phases while refining the diffraction data. The thermal evolution of the lattice parameters is plotted (with respect to the cubic lattice parameter, a_{cub}) in Fig. 8(a). The refined lattice parameter for the cubic phase (at 300 K) is found to be $a_{\text{cub}} = 6.812(6)$ Å, and those for the orthorhombic phase (at 15 K) are found to be $a_{\text{orth}} = 9.766(1)$ Å, $b_{\text{orth}} = 6.582(5)$ Å, and $c_{\text{orth}} = 4.824(1)$ Å. In the case of a cubic-to-orthorhombic structural phase transition, the lattice parameters for the low-temperature (LT) orthorhombic unit cell are associated with the high-temperature (HT) cubic structure by the following relations: $a_{\text{orth}} = \sqrt{2}a_{\text{cub}}$, $b_{\text{orth}} = a_{\text{cub}}$, and $c_{\text{orth}} = a_{\text{cub}}/\sqrt{2}$ [37]. The ratio c/a turns out to be close to 0.75 indicating considerable distortion of the cubic cell as T is lowered. The cell volume around the thermal hysteresis regime changes around 2% between the low- and high-temperature phases, which is similar to the cell volume change of the ferromagnetic (FM) shape memory alloy, Ni₂MnGa [37]. The atomic positions for the cubic and orthorhombic structures are given in Table I. These values are similar to those of other Heusler-based shape memory alloys, such as Co₂NbSn [38] and Ni_{2.04}Mn_{1.4}Sn_{0.56} [39], undergoing a martensitic-type phase transition.

For the 15-K data, there is a finite percentage of the cubic phase present suggesting the coexistence of both the phases even in the low- T region. The variation of the phase fraction consisting of the orthorhombic phase and cubic phase with temperature is presented in Fig. 8(b). An increase in the fraction of the orthorhombic phase along with a decrease in the fraction of the cubic phase with decreasing T can be clearly observed. This observation supports the occurrence of a phase transformation, as also evident from the thermal hysteresis in the ρ vs T data along with the anomaly in the high-temperature C_p data.

V. THEORETICAL RESULTS

A. Density of states

The first-principles electronic structure calculations have been performed for both LT and HT phases of GdPd₂Bi. The

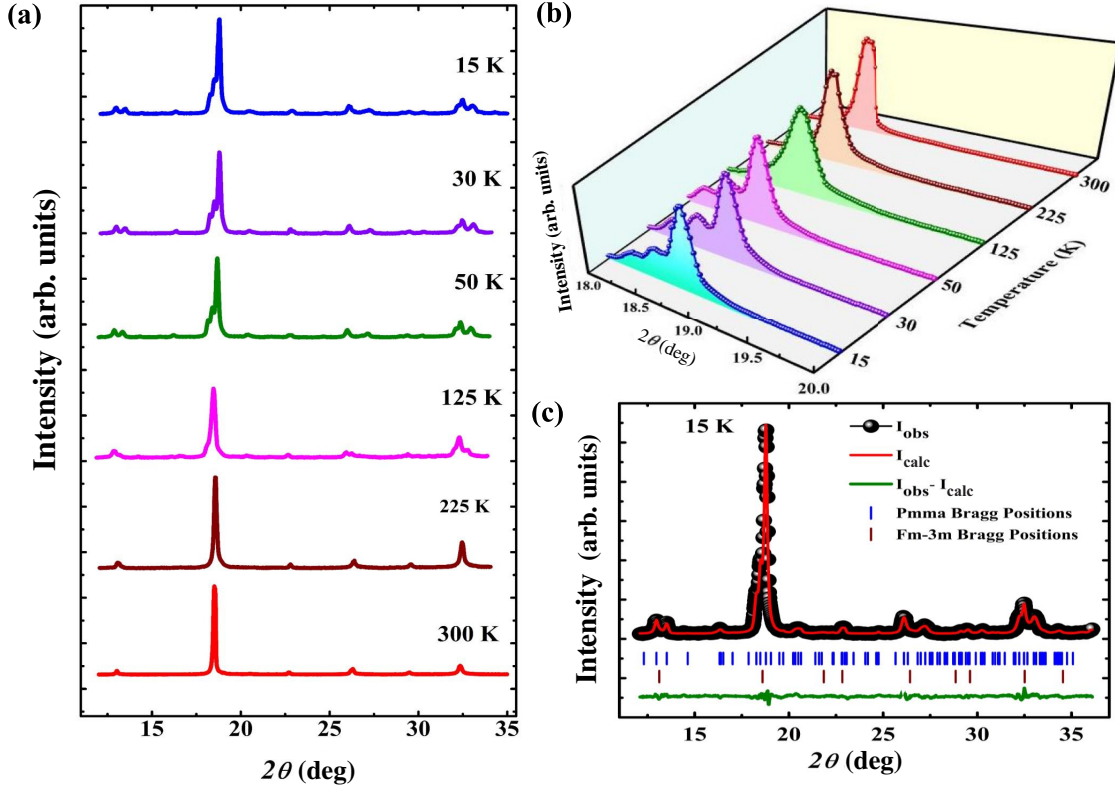


FIG. 7. (a) X-ray diffraction patterns for GdPd₂Bi at various temperatures. (b) Magnified three-dimensional plot for the most intense peak for various temperatures. (c) X-ray diffraction pattern recorded at 15 K; observed intensities (black spheres), calculated intensities (solid red line), and their difference (solid green line), as well as allowed Bragg positions (blue ticks and brown ticks), are marked.

calculated spin-polarized generalized gradient approximation + U_{eff} (GGA + U_{eff}) densities of states (DOSs) are shown in Figs. 9(a) and 9(b) for high- and low-temperature phases of GdPd₂Bi, respectively. From the DOSs, it is clear that both the high- and low-temperature phases are metallic in nature with small but finite DOS contributions at the Fermi energy E_F in both spin channels. The calculated spin magnetic moment at the position of Gd ions per site is $\approx 7.0 \mu_B/\text{site}$ for both high-temperature cubic and low-temperature orthorhombic structures, whereas the induced magnetic moment at the Pd and Bi sites is very small (around $-0.03 \mu_B$). Notably,

the induced moments at the Pd and Bi sites are of opposite sign to the sign of the Gd magnetic moment. The electronic structures of both LT and HT phases have been verified by varying the on-site Coulomb correlations, i.e., U_{eff} from 0 to 6 eV at the Gd site. As the on-site Coulomb correlation increases, the Gd-4*f* states are moving apart as evident in Fig. 9, without opening any gap at the Fermi energy, confirming the robustness of the metallic nature of the electronic structure.

The orbital-projected DOSs in Figs. 9(c) and 9(d) demonstrate that sharp localized peaks are the Gd-4*f* states, which are filled in the majority spin channel and empty in the

TABLE I. Crystallographic parameters of the sample as obtained from the refinement of the PXRD data.

Structure and space group	$L2_1$ cubic $Fm\bar{3}m$					Orthorhombic $Pmma$				
	Cell parameters (\AA)	$a_{\text{cub}} = 6.812(6)$				$a_{\text{orth}} = 9.766(1), b_{\text{orth}} = 6.582(5), c_{\text{orth}} = 4.824(1)$				
Cell volume (\AA^3)	316.24(1)					309.63(5)				
Standard deviation σ_D	1.77					1.56				
Temperature	300 K					15 K				
Atom	Site	x	y	z	B_{iso}	Site	x	y	z	B_{iso}
Gd	4b	$\frac{1}{2}$	$\frac{1}{2}$	$\frac{1}{2}$	0.5(3)	2a	0	0	0	1.1(2)
Pd	8c	$\frac{1}{4}$	$\frac{1}{4}$	$\frac{1}{4}$	0.4(4)	2f	$\frac{1}{4}$	$\frac{1}{2}$	0.509(1)	0.9(1)
		0	0.266(5)	$\frac{1}{2}$		0.7(1)				
		$\frac{1}{4}$	0.265(2)	0.031(9)		0.45(9)				
Bi	4a	0	0	0	1.1(9)	2b	0	$\frac{1}{2}$	0	1.2(1)
		$\frac{1}{4}$	0	0.503(3)		1.1(5)				
		$\frac{1}{4}$	0	0.503(3)		1.1(5)				

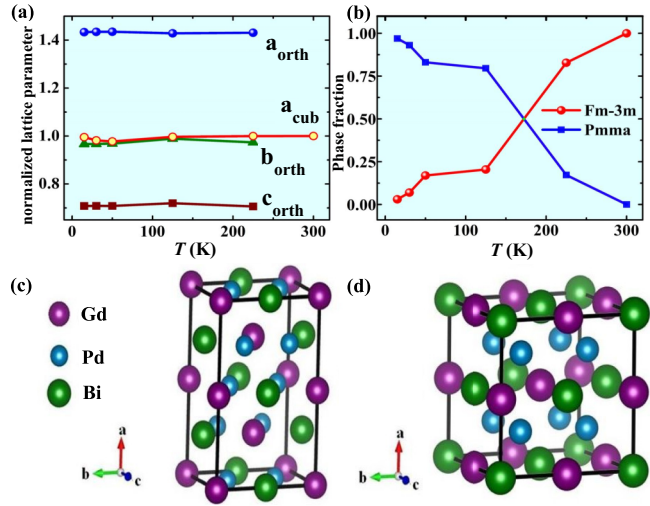


FIG. 8. (a) The thermal variation of lattice parameters (a_{orth} , b_{orth} , c_{orth} , and a_{cub}). (b) Phase fraction (in percent) with temperature. (c) and (d) Crystallographic images of the low- T ($Pmma$) and high- T ($Fm\bar{3}m$) phases, respectively. The solid lines through the data points in (a) and (b) are guides for the eye.

minority spin channel. The empty Gd- $5d$ states are comparatively delocalized and contribute to the metallicity in GdPd₂Bi via the presence at the Fermi energy of the conduction bands. The magnetic moments are primarily originating from the spin splitting of the Gd- $4f$ state ($7.0 \mu_B/\text{site}$), as clearly visible for the DOS in both HT and LT phases. The hybridization between the Gd- $5d$ and Gd- $4f$ states is very weak with almost no overlapped states, except minor overlapping in the empty minority spin channels. These minor overlaps of empty Gd- $4f$ and Gd- $5d$ states induce very small moments of $0.12 \mu_B/\text{site}$ at the Gd- $5d$ states. Therefore, in one way, Gd- $5d$ states are involved in the scattering mechanism of the conduction electrons without being involved in the magnetism of the sys-

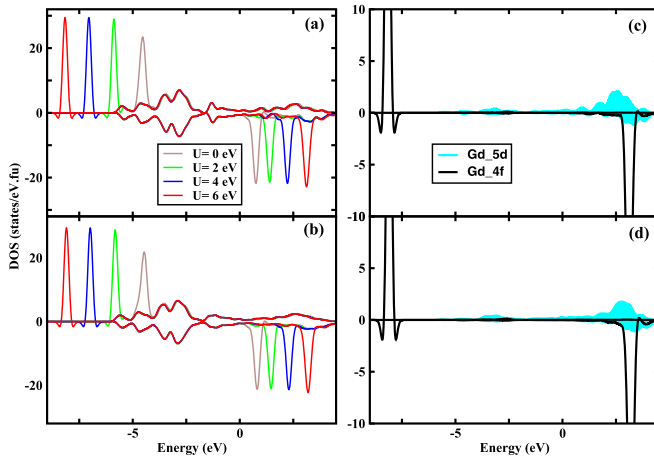


FIG. 9. The calculated spin-polarized total DOS for (a) high temperature and (b) low temperature, for different U_{eff} values. The positive and negative DOS in each panel represent majority and minority spin channels of the DOS. (c) and (d) Comparison of the Gd- $5d$ and Gd- $4f$ states for high temperature and low temperature, respectively. The Fermi level is set at zero in the energy scale.

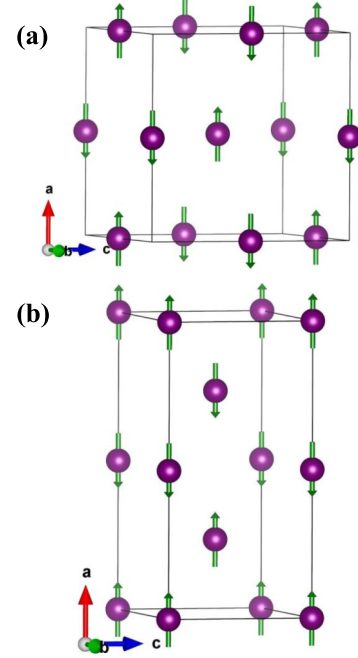


FIG. 10. The pictorial representation of the lowest-energy anti-ferromagnetic spin configurations for (a) HT and (b) LT of GdPd₂Bi in the Gd-only sublattice structure.

tem, whereas the highly localized weakly interacting Gd- $4f$ states provide the magnetic moment via large spin splitting. The large magnetic moments of the $4f$ states get ordered at low temperature through the Ruderman-Kittel-Kasuya-Yosida (RKKY) type of exchange mechanism via the delocalized $5d$ band of conduction electrons. The small mutual overlap of the empty Gd- $5d$ and Gd- $4f$ states opens up a channel of interaction via which the long-range RKKY-type interactions are established.

B. Magnetic configuration

Experimentally, the sample shows an AFM ground state at low temperature along with a negative θ_p in the paramagnetic phase. Therefore it is pertinent to calculate the total energies of different spin configurations for both HT and LT structures. The calculated energetics are shown in Table II. The results show that in both the structures the AFM configuration is energetically lower than the ferromagnetic configuration by 3.77 (2.95) meV/f.u. for HT (LT) structures (as mentioned in Table II). We have calculated various other spin configurations as well. However, the presented spin configurations in Fig. 10 are energetically lower than the other AFM configurations. In the HT cubic structure, the Gd-only sublattice as shown in Fig. 10(a) forms a regular tetrahedral unit with $\uparrow\downarrow\uparrow\downarrow$ spin arrangement. In contrast, in the case of the LT orthorhombic structure, due to reduction of the symmetry, the Gd atoms form an isosceles triangle with AFM arrangement. As a whole, the spins on the Gd atoms are arranged in a parallel manner in the bc plane and coupled in an antiparallel manner along the crystallographic a direction.

TABLE II. Energetics of the different spin configurations of the HT and LT phases of GdPd₂Bi.

Phase	Configuration	Gd1	Gd2	Gd3	Gd4	ΔE (meV)
HT	FM	↑	↑	↑	↑	3.77
	AFM	↑	↓	↑	↓	0.0
LT	FM	↑	↑	↑	↑	2.95
	AFM	↑	↓	↑	↓	0.0

C. Band structure

The robustness of the metallicity and the electronic structure has also been analyzed in the presence of SOC for both HT and LT phases. Figure 11 shows the band structure in the presence of the Coulomb correlation U and the SOC in the AFM ground state spin configurations. From the band structure it is clear that even in the presence of the SOC and AFM correlation, the metallicity is preserved. Moreover, careful investigation reveals that for both the HT [Fig. 11(a)] and LT [Fig. 11(b)] configurations, the valence and conduction bands cross the Fermi energy. For example, in the HT cubic phase, the valence bands cross the Fermi energy in the $X-U$ direction of the BZ, whereas the conduction bands cross the Fermi energy in multiple regions such as $K-\Gamma-L$ and $\Gamma-X$ in the BZ. Similarly, for the LT phases, the conduction bands cross the E_F about the Γ , Z , and Y points in the BZ. However, the valence bands cross the E_F along the $X-\Gamma-Z$, $U-Y$, and $S-T$ directions in the BZ. The bands that cross the Fermi energy dominantly contribute from the Pd-4d and Bi-5p orbitals. The effect of SOC on the magnetic moment is minimal, except that

there is a small orbital magnetic moment at the Gd site of the order of $0.02 \mu_B$.

D. Fermi surface

We have plotted the bandwidth crossing the E_F and the corresponding Fermi surfaces in the presence of SOC for both HT and LT phases in Figs. 12(a) and 12(b), respectively. From the bandwidths, it is clear that both electron pockets and hole pockets are present in both HT and LT phases of the title compound. Careful investigation of Figs. 11 and 12 confirms that the hole pocket is more dominant in the LT phase than in the HT phase. In Fig. 12(a), the bands crossing the Fermi energy and forming electron pockets are predominant in nature. The corresponding Fermi surfaces are also shown in the inset of Fig. 12. It is clear that the electron pocket Fermi surfaces are mainly of three types, whereas the hole pocket Fermi surfaces are of one type, with complicated nesting in the BZ. All the Fermi surface pockets are not located in the BZ following the strict cubic symmetries. Because the shown Fermi surfaces are for each individual band and depend on the dispersion of that particular band in the presence of SOC in the BZ, the location of the Fermi surfaces will be determined. The electron pockets are mostly located around the Γ point, and the hole pockets are at the edge of the BZ near the high-symmetry U and X points. Although there are some hole pockets in the Fermi surface, the dominant carriers are still in the electron pockets in the BZ. The LT case is not exactly same as that of the HT in the context of the carrier pockets in the BZ. In the insets of Fig. 12(b), the Fermi surfaces of the electron and hole pockets are shown for the LT phase; there are a few distinct differences between these Fermi surfaces and those of the HT phase. In the LT phase, we observe an increase in the hole pockets at the expense of the electron pockets. In Fig. 12(b), the hole pockets form two different kinds of Fermi surfaces located around the Γ point and span larger areas in the BZ. Therefore, from the Fermi surface plots, it is clear that in both HT and LT phases, electrons and holes contribute in the carrier type; however, in the LT phase, the hole contributions have increased compared with those of the HT phase.

In addition to the band-resolved three-dimensional Fermi surfaces, we have also calculated the two-dimensional (2D) projected Fermi surface contours plotted in Figs. 12(c) and 12(d). In the HT cubic structure of GdPd₂Bi, there exist bands in close proximity to the X and Γ high-symmetry points at the Fermi level as we can see in the SOC+GGA band structure. We have demonstrated the occurrence of the Fermi surface nesting around these two points within the momentum plane encompassing K_1-K_3 as illustrated in Fig. 12(c). Similarly, we have performed a comparative analysis for the LT orthorhombic structure and depicted the 2D Fermi surface contour plot

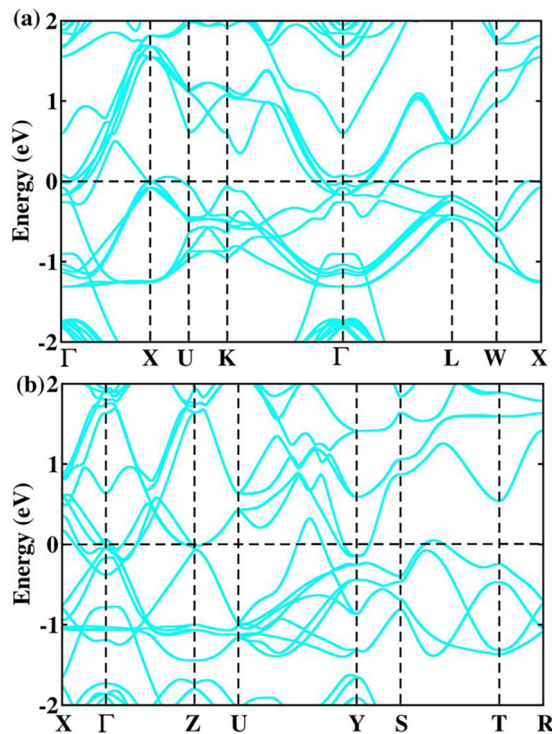


FIG. 11. The calculated spin-polarized GGA + U + SOC band structures along the high-symmetry direction in the Brillouin zone (BZ) for (a) HT and (b) LT of GdPd₂Bi. The Fermi level is set at zero in the energy scale.

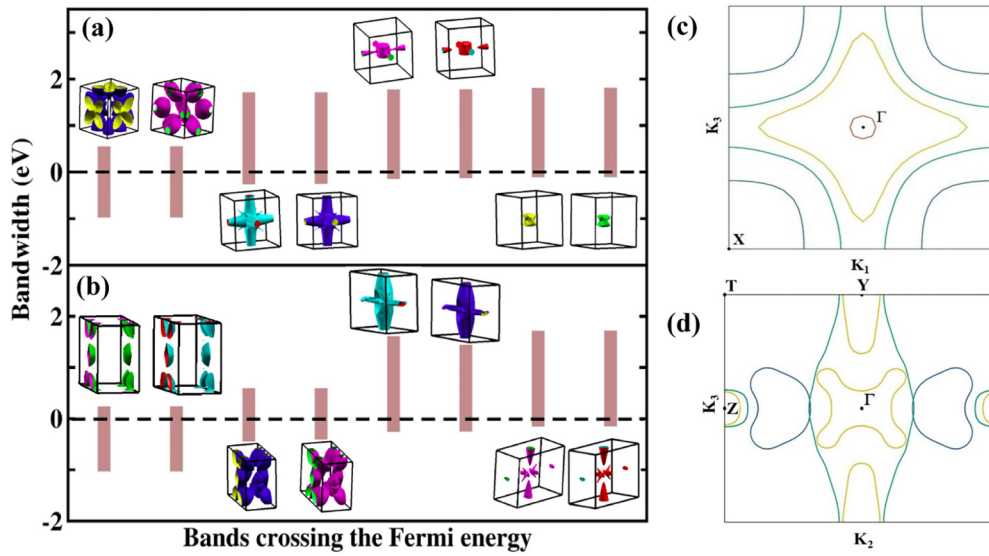


FIG. 12. The calculated GGA + U + SOC bandwidths for (a) HT and (b) LT of GdPd₂Bi are indicated by vertical brown bars which cross the Fermi energy. The corresponding band-resolved Fermi surfaces are shown in the insets. (c) and (d) Two-dimensional contour plots of the Fermi surfaces for HT and LT, respectively.

within the K_2 - K_3 momentum plane. In this case, we have observed the Fermi surface nesting around the N , Γ , and Y points, and an absence of it near the T point, as shown in Fig. 12(d). From the 2D contour plots, it is very clear that the Fermi surface nesting is very different between the HT and LT phases of GdPd₂Bi.

VI. DISCUSSION

The structural transition from a cubic phase to a low-symmetry phase is already reported for RPd_2Bi ($R = Dy, Ho$) [13]. However, Gd with orbital angular momentum $L = 0$ at the ground state is electronically different from the other rare-earth ions. Nevertheless, the observation of a structural phase transition indicates that the orbital moment has little effect on the phenomenon.

GdPd₂Bi depicts thermal hysteresis in the electrical transport measurement around the structural transition. At high temperatures (>200 K), $\rho(T)$ is metallic followed by an upturn below 200 K, and this region of upturn shows thermal hysteresis indicating a first-order phase transition. Evidently, this upturn manifests the structural transition observed in our PXRD data (see Fig. 8). Further evidence in support of the occurrence of a first-order transition is seen from the C_p and α_S versus T data. It is interesting to note that $\rho(T)$ has remarkable similarities with several transition-metal-based shape memory alloys undergoing martensitic phase transition (MPT), where a sharp and hysteretic rise in ρ between two metallic phases is observed. The common examples are Ni-Co-Al, Ni-Mn-Sn, Ni-Mn-In, etc. [37,40–42]. In the case of one such Ni-Mn-Sn alloy (nominal composition, Ni₂Mn_{1.4}Sn_{0.6}), the rise in ρ around the MPT is about 36%, which is comparable to the 43% rise in the presently studied GdPd₂Bi.

The analysis of our T -dependent PXRD data indicates that the sample undergoes a structural transition from cubic ($Fm\bar{3}m$) to orthorhombic ($Pmma$) structure (see Fig. 7).

For GdPd₂Bi, we observe robust Bain distortion [37,43] between cubic and orthorhombic cell parameters: $a_{\text{orth}} = \sqrt{2}a_{\text{cub}}$, $b_{\text{orth}} = a_{\text{cub}}$, and $c_{\text{orth}} = a_{\text{cub}}/\sqrt{2}$. A similar lattice transformation is also observed in the cases of Co₂NbSn, Ni₂Mn_{1.44}Sn_{0.56}, and Ni₂Mn_{1.48}Sb_{0.52} samples across the MPT [38,39]. For GdPd₂Bi, we observe 1.5% change in lattice volume across the transition, although the lattice distortion is significant. MPT is a shear-dominated nondiffusive solid-to-solid phase transition, where the volume change is small [44]. Therefore the observed transition in GdPd₂Bi is likely to be of martensitic type. The MPT in GdPd₂Bi is clearly first order in nature, which is supported by the phenomenon of phase coexistence obtained from our PXRD data [45].

Below 30 K, the resistivity shows a saturating tendency, which eventually turns metallic under the application of H resulting in large negative MR. We observe a non-Fermi-liquid-to-Fermi-liquid (NFL-to-FL) transition in the resistivity data as H is increased above 20 kOe. The temperature window for the FL state ($\rho \sim T^2$) increases with increasing H . A similar field-induced transition from a NFL to a FL is observed in other systems, such as the heavy-fermion (HF) material YbCu_{5-x}Au_x [46], the HF superconductor CeCoIn₅ [47], and even cuprate superconductors [48]. The NFL-to-FL transition is attributed to the suppression of the AFM spin fluctuations. For GdPd₂Bi, T_N is close to 9 K, and it moves to lower T with increasing H (see C_p data in Fig. 3); a similar mechanism can be present here.

The observed negative MR follows an H^2 dependence up to 150 kOe of field in GdPd₂Bi, and it remains unsaturated. The negative MR is prevalent in the PM phase (~ 120 K) well above the AFM transition temperature. There are reports of negative MR in several other intermetallic AFM compounds in the PM phase, such as Gd₂PdSi₃, GdNi₂Si₂, FeSe₂, and so on [49–51]. For GdNi₂Si₂, negative MR is found both in the PM ($T \gtrsim T_N$) state and also below T_N varying almost quadratically with H . Such behavior cannot be attributed to

the Kondo effect due to the well-localized character of Gd-4*f* electrons, but rather depends on the spin fluctuations in the Ni-3*d* band [50]. The negative MR close to T_N arises due to the suppression of spin fluctuations by the magnetic field. However, for some compounds (e.g., Gd₂PdSi₃), considerable MR exists well above T_N , and it is attributed to the formation of magnetic polarons. The applied field aligns these magnetic polarons (local FM clusters) leading to the reduction of spin-dependent scattering [49].

In the case of GdPd₂Bi, one is quite unlikely to observe AFM fluctuations at temperatures much higher than T_N . A polaronic picture can also be mooted for GdPd₂Bi, similar to Gd₂PdSi₃. The formation of magnetic polarons can be manifested in $\chi(T)$ measurements from the downturn in the inverse susceptibility plot associated with the deviation from the Curie-Weiss fit. However, the magnetic susceptibility of GdPd₂Bi shows a perfect Curie-Weiss behavior down to about 15 K, and the data recorded at $H = 100$ Oe and 1 kOe overlap with each other [see inset of Fig. 1(b)]. Also, the θ_p obtained is negative with a value of -18 K, indicating the lack of ferromagnetic (FM) correlations. It is to be noted that the $M(H)$ curves are strictly linear for $T = 5, 10,$ and 150 K, ruling out any short-range FM correlations. In addition, a common feature of negative MR due to magnetic polarons is the sharp increase in the MR at low magnetic fields [52,53]. Additionally, had the MR been related to the spin fluctuation or magnetic polarons, one would expect a saturation or tendency towards saturation at higher fields. Also, the value of negative MR is expected to be maximum at the magnetic transition temperature and diminish on both sides of it. However, in GdPd₂Bi, the negative MR decreases monotonically with increasing temperature. Also, we observe a robust H^2 behavior even at a field as high as 150 kOe. At such a high field, the spin fluctuation should get completely suppressed, or the polarons would have melted. Therefore a simple spin-fluctuation or polaronic model may not be appropriate here.

A nonsaturating positive MR varying quadratically with H is not uncommon. There are several systems having nontrivial topology in their electronic structure, which show nonsaturating positive MR [54–58]. The presently studied compound does not belong to that category as it has a centrosymmetric crystal structure in both its HT ($Fm\bar{3}m$) and LT ($Pmma$) phases and its MR is negative.

Therefore the high-temperature negative MR in GdPd₂Bi turns out to be rather puzzling. We found a few other Gd-based compounds in the literature, such as GdI₂, Gd₂Ni₂Cd, and GdSi, showing negative MR in the PM state [59–61]. Although the magnitude of MR is much smaller in GdPd₂Bi, it qualitatively resembles the features observed in the above-mentioned Gd compounds. Among them, GdI₂ is well studied for its electronic structure. The negative MR in GdI₂ is assigned to *s-f* interaction between the delocalized 5*d* and the localized 4*f* levels. Fermi surface nesting also plays an important part in the MR behavior. In our spin-polarized DOS calculation [Figs. 9(c) and 9(d)], we find negligible overlap of the 4*f* and the 5*d* electrons below E_F , while there is a large overlap of the minority 4*f* spin channel with the 5*d* level above E_F . Such overlap may contribute to the polarization of the 5*d* electrons, and it is pivotal in contributing to the RKKY interaction.

The localized 4*f* moments in GdI₂ tend to get aligned in the direction of H under an applied magnetic field. Due to the finite *s-f* interaction, minority 5*d* levels above E_F get shifted in the majority 5*d* band just below E_F . In other words, the 5*d* level gets spin polarized. Since 5*d* electrons are responsible for electrical conduction, the spin polarization reduces the magnetic scattering, and a negative MR is seen even in the PM state. A similar *s-f* interaction model is also mooted for Gd₂Ni₂Cd and GdSi.

GdPd₂Bi has nested Fermi surfaces [see the contour plots in Figs. 12(c) and 12(d)] and small but finite 5*d*-4*f* overlap. Considering these facts, we propose that the negative MR in the PM phase originates from the polarization of 5*d* levels by the 4*f* moment. Interestingly, Yamada and Takada proposed a theoretical model based on the first Born approximation in rare-earth systems due to the interaction of conduction electrons and the 4*f* moment in the case of AFM metals [62,63]. They found that above the Néel temperature, MR is negative, and it varies as H^2 , which exactly matches with our results. This strengthens our conjecture of the *s-f* interaction contributing to the negative MR in the PM state of GdPd₂Bi.

GdPd₂Bi shows a martensitic transition, and it may contain martensitic variants at low temperature [64]. It has been found (especially in the case of ferromagnetic shape memory alloys) that a magnetic field can induce a reverse transition from martensite to austenite leading to negative MR. However, for GdPd₂Bi, we found that the martensitic transition temperature is completely insensitive to H , and therefore such a phenomenon can be ruled out.

At this point, it is worth comparing the physical properties of two closely related compounds, namely, HoPd₂Bi and ErPd₂Bi, with GdPd₂Bi. The Ho compound is AFM below ~ 5 K, and the Er compound does not order down to 2 K. Both the Ho compound and the Er compound show a structural transition below about 200 K. Kaczorowski *et al.* [25] and Gofryk *et al.* [13] have attributed the structural transition to reconstruction of the electronic band structure. It is interesting to note that the Sb counterparts (namely, RPd_2Sb with $R = Ho, Er$) do not undergo a structural transition. Therefore Bi plays an important role in the structural instability.

The α_S value for GdPd₂Bi is negative for $T \geq 25$ K and positive below it. Interestingly, the sign of R_H is negative, indicating electrons to be the dominant charge carrier in GdPd₂Bi, which is in line with α_S . However, below about 30 K, ρ_{xy} turns nonlinear indicating the significant contribution of holes in addition to electrons in the system. It might be possible that the contribution from the holes become significant for $T < 30$ K, which in turn leads to small positive values of α_S . The Fermi surface plots (see Fig. 12) show that two types of carriers (i.e., electron and hole) exist in the HT and LT phases. However, in the LT phase, the hole contribution as a carrier is more prominent than in the HT phase. This might be the reason for the positive sign of α_S at low temperature and the observed nonlinearity in the $\rho_{xy}(H)$ data.

The n vs T plot [see Fig. 5(b)] drops with decreasing temperature below 200 K, in the regime where the anomalies are observed in the $\rho(T)$ and $C_P(T)$ data. This points to the change in electronic concentration across the MPT. The theoretical calculations indicate that the contribution from the hole pocket is more prevalent in the LT phase than in the HT phase.

On the other hand, the electron pockets are predominant in nature in the HT phase. This corroborates the increase in electronic concentration with temperature across the structural transition between the HT and LT phases.

Nonlinearity in ρ_{xy} below T_N may also arise from the anomalous Hall effect (AHE) contribution [12], and the presence of the AHE cannot be completely discarded in the present case. In recent years, Weyl semimetals have been reported to show a large AHE owing to their unique band topology due to having either broken inversion symmetry (IS) or broken time-reversal symmetry (TRS) [65]. GdPd₂Bi crystallizes in a cubic $L2_1$ structure which is centrosymmetric in nature. The LT orthorhombic phase with space group $Pmma$ is also centrosymmetric. This rules out the broken inversion symmetry picture in both high- and low- T phases.

The only other possibility for the occurrence of the AHE is broken TRS. Various Co-based high- T_C ferromagnetic full-Heusler compounds have recently been reported to show a large AHE due to broken TRS (for example, Co₂FeGe, Co₂FeAl, Co₂TiSn, Co₂TiGe, and many more) [5]. The broken TRS in GdPd₂Bi may occur only below $T_N \sim 9$ K, while the nonlinearity in the $\rho_{xy}(H)$ data is present even at 30 K (see Fig. 6). So, we can rule out the role of broken TRS in the nonlinear Hall effect. Even if we assume that the nonlinearity in ρ_{xy} occurs from the AHE in GdPd₂Bi and calculate the value from high-field extrapolation of $\rho_{xy}(H)$ data (not shown here), it comes out to be very low ($\rho_{xy}^{\text{AHE}} = 0.01$ and $0.0125 \mu\Omega \text{ cm}$ for $T = 5$ and 10 K, respectively). This prompts us to believe that a two-carrier model [31,66–68] is more appropriate to understand nonlinear ρ_{xy} and other anomalies.

VII. SUMMARY AND CONCLUSIONS

An in-depth study of the structure and magnetic and electronic ground state of the full-Heusler GdPd₂Bi compound

is presented via x-ray diffraction, magnetization, magnetotransport, thermal transport, and heat capacity measurements with further support from DFT calculations. The magnetic study reveals that the compound orders antiferromagnetically at around 9 K. The total energy calculations further confirm that the AFM correlation is dominant over the fully polarized spin configuration for GdPd₂Bi. The magnetotransport study reveals uncharacteristic thermal hysteresis in the 100–200 K range, while no corresponding singularities are observed in the magnetic data. In addition, a fairly high quadratic and nonsaturating magnetoresistance has been observed in this compound. We propose that the negative MR is associated with the polarization of $5d$ conduction electrons by the localized $4f$ moment in the presence of nested Fermi surfaces similar to GdI₂ and a few other Gd-based metals. Our analyses reveal that a martensitic-type structural phase transition is likely to be associated with the thermal hysteresis, and no gap opening occurs at E_F for either the HT or LT phase.

ACKNOWLEDGMENTS

S.C., P.D., and S.S. would like to acknowledge the University Grants Commission (India), the Science and Engineering Research Board (Grant No. PDF/2017/001061), and IIT Goa, respectively, for support from their research fellowships. S.K. thanks the Department of Science and Technology, Government of India, for providing an INSPIRE faculty research grant (Grant No. DST/INSPIRE/04/2016/000431; IFA16-MS91). The UGC DAE-CSR Indore and Kolkata centers, where the low-temperature transport and heat-capacity measurements were performed, are duly acknowledged. The authors would like to sincerely acknowledge the Indian beam-line facility at Photon Factory, KEK, Tsukuba, Japan, where the low-temperature synchrotron x-ray diffraction measurements were performed.

-
- [1] B. R. K. Nanda and I. Dasgupta, *J. Phys.: Condens. Matter* **15**, 7307 (2003).
- [2] T. Graf, C. Felser, and S. S. P. Parkin, *Prog. Solid State Chem.* **39**, 1 (2011).
- [3] K. Özdoğan, E. Şaşıoğlu, and I. Galanakis, *J. Appl. Phys.* **113**, 193903 (2013).
- [4] T. Krenke, E. Duman, M. Acet, E. F. Wassermann, X. Moya, L. Mañosa, and A. Planes, *Nat. Mater.* **4**, 450 (2005).
- [5] S. Chatterjee, S. Chatterjee, S. Giri, and S. Majumdar, *J. Phys.: Condens. Matter* **34**, 013001 (2022).
- [6] M. Ishikawa, J. L. Jorda, and A. Junod, in *Superconductivity in d- and f-Band Metals: Proceedings of the IV International Conference* (Kernforschungszentrum Karlsruhe, Karlsruhe, Germany, 1982), p. 141.
- [7] M. J. Johnson and R. N. Shelton, *Solid State Commun.* **52**, 839 (1984).
- [8] S. K. Malik, A. M. Umarji, and G. K. Shenoy, *Phys. Rev. B* **31**, 6971 (1985).
- [9] H. Lin, L. A. Wray, Y. Xia, S. Xu, S. Jia, R. J. Cava, A. Bansil, and M. Z. Hasan, *Nat. Mater.* **9**, 546 (2010).
- [10] W. Al-Sawai, H. Lin, R. S. Markiewicz, L. A. Wray, Y. Xia, S.-Y. Xu, M. Z. Hasan, and A. Bansil, *Phys. Rev. B* **82**, 125208 (2010).
- [11] C. Shekhar, S. Ouardi, A. K. Nayak, G. H. Fecher, W. Schnelle, and C. Felser, *Phys. Rev. B* **86**, 155314 (2012).
- [12] C. Shekhar, N. Kumar, V. Grinenko, S. Singh, R. Sarkar, H. Luetkens, S.-C. Wu, Y. Zhang, A. C. Komarek, E. Kampert, Y. Skourski, J. Wosnitzer, W. Schnelle, A. McCollam, U. Zeitler, J. Kübler, B. Yan, H.-H. Klauss, S. S. P. Parkin, and C. Felser, *Proc. Natl. Acad. Sci. USA* **115**, 9140 (2018).
- [13] K. Gofryk, D. Kaczorowski, T. Plackowski, A. Leithe-Jasper, and Yu. Grin, *Phys. Rev. B* **72**, 094409 (2005).
- [14] K. Gofryk, Thermoelectric properties $4f$ and $5f$ -Heusler electronic phases RPdX and RPd₂X (X = Sb and Bi), Institute of Low Temperature and Structure Research, Polish Academy of Sciences, Wrocław, Poland, 2005.
- [15] <https://luttero.github.io/maud/>.
- [16] G. Kresse and J. Hafner, *Phys. Rev. B* **47**, 558(R) (1993).
- [17] G. Kresse and J. Furthmüller, *Phys. Rev. B* **54**, 11169 (1996).
- [18] J. P. Perdew, K. Burke, and M. Ernzerhof, *Phys. Rev. Lett.* **77**, 3865 (1996).

- [19] V. I. Anisimov, I. V. Solovyev, M. A. Korotin, M. T. Czyzyk, and G. A. Sawatzky, *Phys. Rev. B* **48**, 16929 (1993).
- [20] S. L. Dudarev, G. A. Botton, S. Y. Savrasov, C. J. Humphreys, and A. P. Sutton, *Phys. Rev. B* **57**, 1505 (1998).
- [21] S. Chatterjee, P. Dutta, S. Giri, S. Majumdar, S. Sadhukhan, S. Kanungo, S. Chatterjee, M. M. Patidar, G. S. Okram, and V. Ganesan, *Phys. Rev. B* **102**, 214443 (2020).
- [22] K. A. Gschneidner, Jr. and V. K. Pecharsky, *J. Rare Earths* **24**, 641 (2006).
- [23] H. Goldsmid, *Thermoelectric Refrigeration* (Temple, London, 1964).
- [24] C. Candolfi, A. Ormeci, U. Aydemir, M. Baitinger, N. Oeschler, Yu. Grin, and F. Steglich, *Phys. Rev. B* **84**, 205118 (2011).
- [25] D. Kaczorowski, K. Gofryk, T. Plackowski, A. Leithe-Jasper, and Yu. Grin, *J. Magn. Magn. Mater.* **290-291**, 573 (2005).
- [26] K. Gofryk, D. Kaczorowski, T. Plackowski, A. Leithe-Jasper, and Yu. Grin, *Phys. Rev. B* **84**, 035208 (2011).
- [27] A. C. Melissinos and J. Napolitano, *Experiments in Modern Physics* (Academic Press, San Diego, CA, 1966).
- [28] S. U. Jen, B. L. Chao, and C. C. Liu, *J. Appl. Phys.* **76**, 5782 (1994).
- [29] A. Laha, R. Singha, S. Mardanya, B. Singh, A. Agarwal, P. Mandal, and Z. Hossain, *Phys. Rev. B* **103**, L241112 (2021).
- [30] J. Honig and T. Harman, *Adv. Energy Convers.* **3**, 529 (1963).
- [31] G. Pokharel, S. M. L. Teicher, B. R. Ortiz, P. M. Sarte, G. Wu, S. Peng, J. He, R. Seshadri, and S. D. Wilson, *Phys. Rev. B* **104**, 235139 (2021).
- [32] Y. Yang, Y. Fu, W. Zhu, J. He, B. Liu, C. B. Liu, L. Li, C. Niu, and Y. Luo, *J. Phys.: Condens. Matter* **34**, 315701 (2022).
- [33] F. G. Aliev, *Phys. B (Amsterdam)* **171**, 199 (1991).
- [34] I. M. Tsidilkovski, *Electron Spectrum of Gapless Semiconductors*, Springer Series in Solid-State Sciences Vol. 116 (Springer, Berlin, 1996).
- [35] H. T. Stokes, D. M. Hatch, and B. J. Campbell, ISODISTORT, ISOTROPY Software Suite, <https://iso.byu.edu/iso/isodistort.php>.
- [36] B. J. Campbell, H. T. Stokes, D. E. Tanner, and D. M. Hatch, *J. Appl. Cryst.* **39**, 607 (2006).
- [37] P. J. Brown, A. P. Gandy, K. Ishida, R. Kainuma, T. Kanomata, K.-U. Neumann, K. Oikawa, B. Ouladdiaf, and K. R. A. Ziebeck, *J. Phys.: Condens. Matter* **18**, 2249 (2006).
- [38] K.-U. Neumann, T. Kanomata, B. Ouladdiaf, and K. R. A. Ziebeck, *J. Phys.: Condens. Matter* **14**, 1371 (2002).
- [39] J. Sannigrahi, S. Pramanick, S. Chatterjee, J. S. Lord, D. Khalyavin, A. D. Hillier, D. T. Adroja, and S. Majumdar, *Phys. Rev. B* **99**, 224401 (2019).
- [40] P. J. Brown, A. P. Gandy, R. Kainuma, T. Kanomata, K. U. Neumann, K. Oikawa, B. Ouladdiaf, A. Sheikh, and K. R. A. Ziebeck, *J. Phys.: Condens. Matter* **23**, 456004 (2011).
- [41] S. Chatterjee, S. Giri, S. Majumdar, and S. K. De, *Phys. Rev. B* **77**, 224440 (2008).
- [42] S. Chatterjee, M. Thakur, S. Giri, S. Majumdar, A. K. Deb, and S. K. De, *J. Alloys Compd.* **456**, 96 (2008).
- [43] S. Singh, B. Dutta, S. W. D'Souza, M. G. Zavareh, P. Devi, A. S. Gibbs, T. Hickel, S. Chadov, C. Felser, and D. Pandey, *Nat. Commun.* **8**, 1006 (2017).
- [44] V. A. Chernenko, *Scr. Mater.* **40**, 523 (1999).
- [45] S. B. Roy, G. K. Perkins, M. K. Chattopadhyay, A. K. Nigam, K. J. S. Sokhey, P. Chaddah, A. D. Caplin, and L. F. Cohen, *Phys. Rev. Lett.* **92**, 147203 (2004).
- [46] P. Carretta, R. Pasero, M. Giovannini, and C. Baines, *Phys. Rev. B* **79**, 020401(R) (2009).
- [47] J. Paglione, M. A. Tanatar, D. G. Hawthorn, E. Boaknin, R. W. Hill, F. Ronning, M. Sutherland, L. Taillefer, C. Petrovic, and P. C. Canfield, *Phys. Rev. Lett.* **91**, 246405 (2003).
- [48] T. Shibauchi, L. Krusin-Elbaum, M. Hasegawa, Y. Kasahara, R. Okazaki, and Y. Matsuda, *Proc. Natl. Acad. Sci. USA* **105**, 7120 (2008).
- [49] R. Mallik, E. V. Sampathkumaran, M. Strecker, and G. Wortmann, *Europhys. Lett.* **41**, 315 (1998).
- [50] E. V. Sampathkumaran and I. Das, *Phys. Rev. B* **51**, 8631 (1995).
- [51] H. Liu and Y. Xue, *Adv. Mater.* **33**, 2008456 (2021).
- [52] W. Shon, J.-S. Rhyee, Y. Jin, and S.-J. Kim, *Phys. Rev. B* **100**, 024433 (2019).
- [53] Y. Zhang, K. Deng, X. Zhang, M. Wang, Y. Wang, C. Liu, J.-W. Mei, S. Kumar, E. F. Schwier, K. Shimada, C. Chen, and B. Shen, *Phys. Rev. B* **101**, 205126 (2020).
- [54] M. Ali, J. Xiong, S. Flynn, J. Tao, Q. D. Gibson, L. M. Schoop, T. Liang, N. Haldolaarachchige, M. Hirschberger, N. P. Ong, and R. J. Cava, *Nature (London)* **514**, 205 (2014).
- [55] C. Shekhar, A. Nayak, Y. Sun, M. Schmidt, M. Nicklas, I. Leermakers, U. Zeitler, Y. Skourski, J. Wosnitza, Z. Liu, Y. Chen, W. Schnelle, H. Borrmann, Y. Grin, C. Felser, and B. Yan, *Nat. Phys.* **11**, 645 (2015).
- [56] B. Wu, V. Barrena, F. Mompeán, M. Garcia-Hernández, H. Suderow, and I. Guillamón, *Phys. Rev. B* **101**, 205123 (2020).
- [57] Z. Li, Y. Zeng, J. Zhang, M. Zhou, and W. Wu, *Phys. Rev. B* **98**, 165441 (2018).
- [58] Y. Li, L. Li, J. Wang, T. Wang, X. Xu, C. Xi, C. Cao, and J. Dai, *Phys. Rev. B* **94**, 121115(R) (2016).
- [59] C. Felser, K. Ahn, R. K. Kremer, R. Seshadri, and A. Simon, *J. Solid State Chem.* **147**, 19 (1999).
- [60] F. Canepa, S. Cirafici, F. Merlo, M. Pani, and C. Ferdeghini, *J. Magn. Magn. Mater.* **195**, 646 (1999).
- [61] H. Li, Y. Xiao, B. Schmitz, J. Persson, W. Schmidt, P. Meuffels, G. Roth, and T. Brückel, *Sci. Rep.* **2**, 750 (2012).
- [62] H. Yamada and S. Takada, *Prog. Theor. Phys.* **49**, 1401 (1973).
- [63] H. Yamada and S. Takada, *J. Phys. Soc. Jpn.* **34**, 51 (1973).
- [64] B. Kiefer and D. C. Lagoudas, *Philos. Mag.* **85**, 4289 (2005).
- [65] S. Onoda, N. Sugimoto, and N. Nagaosa, *Phys. Rev. Lett.* **97**, 126602 (2006).
- [66] T. Ogasawara, K.-K. Huynh, T. Tahara, T. Kida, M. Hagiwara, D. Arçon, M. Kimata, S. Y. Matsushita, K. Nagata, and K. Tanigaki, *Phys. Rev. B* **103**, 125108 (2021).
- [67] C. Schindler, S. Galeski, W. Schnelle, R. Wawrzynczak, W. Abdel-Haq, S. N. Guin, J. Kroder, N. Kumar, C. Fu, H. Borrmann, C. Shekhar, C. Felser, T. Meng, A. G. Grushin, Y. Zhang, Y. Sun, and J. Gooth, *Phys. Rev. B* **101**, 125119 (2020).
- [68] S. Lei, J. Lin, Y. Jia, M. Gray, A. Topp, G. Farahi, S. Klemenz, T. Gao, F. Rodolakis, J. L. McChesney, C. R. Ast, A. Yazdani, K. S. Burch, S. Wu, N. P. Ong, and L. M. Schoop, *Sci. Adv.* **6**, eaay6407 (2020).